



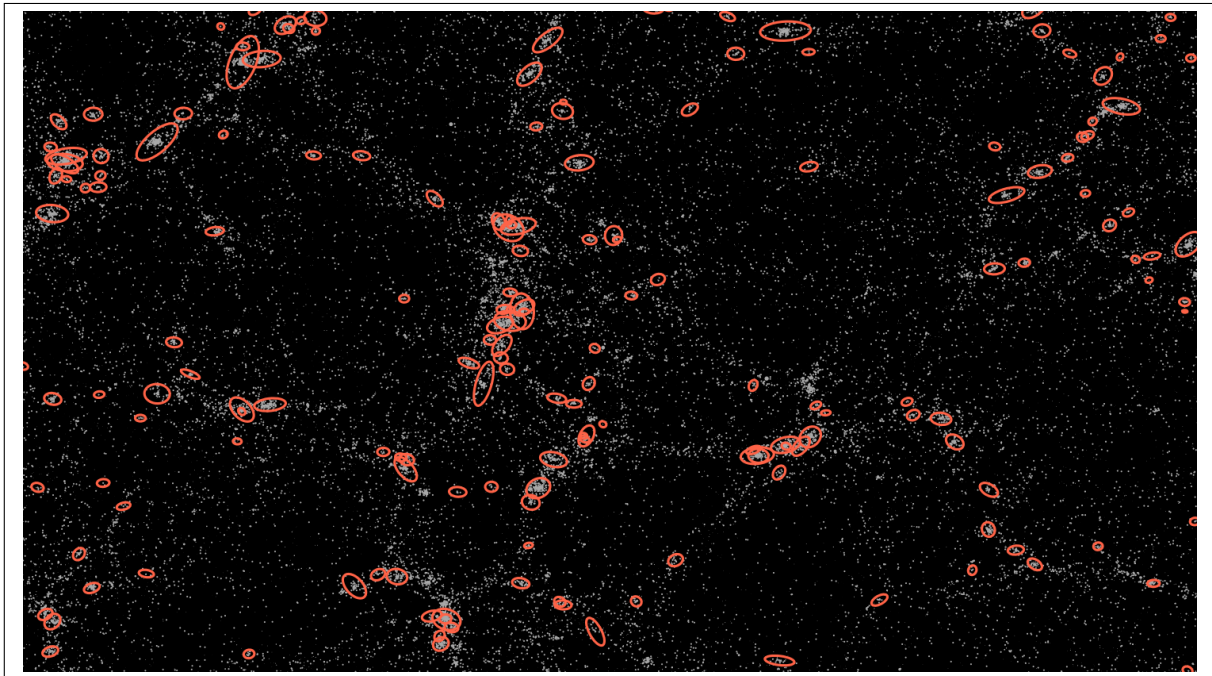
Universiteit Utrecht

Physics & Astronomy
UCU Liberal Arts & Sciences

Mitigating intrinsic alignment impact on spectroscopic surveys

BACHELOR THESIS

Karel Zwetsloot



Supervisor:

Dr. N.E. Chisari
Institute for Theoretical Physics

16/06/2021

Abstract

Galaxy clustering statistics are an increasingly important observational probe of the large-scale structure of the Universe, especially because of their ability to constrain the growth rate through RSD effects. As a new generation of spectroscopic surveys is expected to bring a much higher degree of precision in our data, we will have to become more sensitive to potential sources of error in our analyses. Galaxy intrinsic alignment effects are typically neglected in galaxy clustering studies, but in recent years it has become apparent that such alignments are likely to contaminate our measurements of the growth rate through an orientation-dependent selection effect. In this thesis we investigate, using a Fisher forecast, how well this selection effect can be mitigated using intrinsic alignment statistics. Our results indicate that the selection effect is significant and that it cannot be resolved using the galaxy clustering power spectrum alone. However, we find that by adding intrinsic alignment statistics, most notably the galaxy-shape power spectrum, the effect can be mitigated effectively and we can still achieve good constraints on the growth rate. This implies that future studies aiming to constrain the growth rate through RSD measurements would benefit from a combined analysis of galaxy clustering and intrinsic alignment statistics.

The front page image is a snapshot of the large-scale structure from the Horizon-AGN simulation, which is a cosmological hydrodynamical simulation of galaxy formation. The red ellipses represent galaxies, and it is even visible by eye that they align towards each other. The white dots represent matter overdensities, including dark matter. The width of the simulation box is 100 Mpc h^{-1} and the snapshot is projected over 25 Mpc h^{-1} . Credit: N.E. Chisari, Horizon-AGN simulation, <https://www.horizon-simulation.org/>.

Contents

1	Introduction	1
2	Theory	2
2.1	The cosmological model: the story of our Universe	2
2.1.1	Hubble expansion	2
2.1.2	The early Universe and the CMB	3
2.1.3	The growth of structure	4
2.1.4	The Λ CDM model	6
2.2	Observational probes	7
2.2.1	Correlation functions and power spectra	8
2.2.2	Redshift space distortions	10
2.3	Intrinsic alignments	12
2.3.1	Linear alignment model	12
2.3.2	Alignment power spectra	13
2.3.3	Selection effects	14
2.3.4	Relationship between A and \tilde{C}_1	16
3	Method	17
3.1	Multipole expansion	18
3.2	Fisher forecast	18
3.2.1	Fisher formalism	19
3.2.2	Fisher matrix for cosmological observables	20
3.3	Fiducial model	21
4	Results	22
4.1	Without selection effect	22
4.2	With selection effect	24
4.2.1	Prior on \tilde{C}_1	24
4.2.2	Adding $P_{EE}^{(0)}$	24
4.2.3	Adding $P_{gE}^{(0)}$	25
4.2.4	Adding both $P_{EE}^{(0)}$ and $P_{gE}^{(0)}$	25
5	Discussion	25
5.1	Interpretation of results	26
5.2	Further considerations	27
6	Conclusion	28

1 Introduction

Questions regarding the origin, history, and evolution of the Universe have fascinated humans ever since we started observing the night sky. Over time we have learned a great deal about these questions, and our current best cosmological model, known as the Λ CDM model, is able to explain many of the key characteristic properties of the Universe observed today. One of these properties is the expansion of the Universe, which leads us to believe that the early Universe was a much hotter and denser place than it is today, and that it started with a Big Bang. In this hot and dense Universe, different forms of energy were mixed together in a big ‘cosmic soup’. The energy components of the Universe seem to be radiation and ordinary (baryonic) matter, but also dark matter and dark energy (Ryden, 2017). We know the latter two exist but their exact nature remains mysterious and is the subject of many scientific collaborations such as LSST DESC et al. (2018).

We also observe structure in the Universe; matter is not uniformly distributed across space but is clumped together to form planets, stars, solar systems, and galaxies. On even larger scales, we see that also galaxies are clustered together to form galaxy clusters, voids, and filaments, for example. This *large-scale structure* is very interesting to cosmologists because it holds valuable information about how the Universe evolved over time, which in turn helps us constrain our cosmological model parameters or learn more about the nature of dark matter and energy. The large-scale structure is intimately tied to the conditions of the early Universe because the seeds of the structure we see today come from small density fluctuations in the ‘cosmic soup’, which by gravitational instability grew over time (Dodelson and Schmidt, 2020).

We have developed various observational probes through which we can access the valuable information that the large-scale structure holds. In this thesis our primary interest is galaxy clustering statistics, by which we mean the statistical properties of the galaxy density field in the Universe. These clustering statistics are typically used to constrain the growth rate, an important cosmological parameter which describes how density perturbations evolve over time (see for example Gil-Marín et al. (2016)). Besides correlations between galaxy positions, we find that also the shapes and orientations of galaxies are correlated with one another; these are known as intrinsic alignments (Catelan et al., 2001). These intrinsic alignment effects are typically not taken into account in galaxy clustering studies, but in Hirata (2009) they show that they could contaminate measurements of the growth rate. This is because 1) galaxy intrinsic alignments are not random and 2) there is a selection bias towards galaxies which are aligned along the line of sight. The distortion is such that it cannot be mitigated using galaxy clustering statistics alone, but the significance of this contamination is still somewhat unclear; it has been detected by some studies (Martens et al., 2018), while others (Singh et al., 2020) have challenged its importance.

In this thesis, we explore how we can mitigate the impact of galaxy intrinsic alignments on spectroscopic surveys due to an orientation-dependent selection effect. Specifically, we investigate how intrinsic alignment statistics, in addition to galaxy clustering statistics, can help constrain the growth rate despite the selection effect. This is done through a Fisher forecast, which allows us to predict how well model parameters can be constrained given certain observables. We find that although the selection effect is significant and needs to be taken into account, it can be integrated into the analysis and mitigated effectively by

including appropriate intrinsic alignment statistics.

This thesis is organized as follows. In section 2 the underlying theory needed to understand this research is discussed. This is split into a section on the current cosmological model (2.1), one on observational probes (2.2), and one on intrinsic alignments and their effect on galaxy clustering statistics (2.3). In section (3) the methods used are discussed, in particular the multipole expansion (3.1) and the Fisher forecast formalism (3.2). Section 4 describes the results for the different scenarios, split into a case where we neglect the selection effect (4.1), and cases where we include it and explore how it could be mitigated (4.2). In section 5, the results are interpreted (5.1) and further considerations are discussed (5.2). Lastly, we conclude the thesis in section 6 and discuss the outlook for further research.

2 Theory

2.1 The cosmological model: the story of our Universe

Before delving into the specific theoretical concepts needed to understand intrinsic alignments and their effect on galaxy clustering surveys, it is worthwhile to review some more fundamental concepts underlying our current cosmological model. This will help place this piece of research into context and highlight its wider importance in fine-tuning our understanding of the Universe. The next two sections (2.1.1 and 2.1.2) are largely based on Ryden (2017) (Chapters 2 & 8).

2.1.1 Hubble expansion

There are a few key characteristics of the Universe that form the basis of our current models. First and foremost we assume that, *on large scales*, the Universe is isotropic and homogeneous. By isotropic we mean that it looks the same no matter in which direction we look; there is no preferred or special *direction*. By homogeneous we mean that it is the same no matter where we are located; there are no preferred or special *locations* either. Note that this is indeed only valid for very large scales ($\sim 100\text{Mpc}$), as one can easily verify that on smaller scales there are significant anisotropies and inhomogeneities: the density on the scale of our solar system is far from uniform, for example, with extremely large densities in the Sun and other planets compared to the voids in between. The next key characteristic is the fact that the Universe is expanding, which is now generally accepted but this has only become apparent in recent decades. Before then, the consensus was that the Universe is instead static. Although celestial objects might have relative velocities with respect to one another, known as *peculiar velocities*, it was believed that there was no overall expansion or contraction. This view was challenged by new data being collected on the *redshifts* of various galaxies, which allows us to estimate their radial velocity.

When electromagnetic sources move with respect to us with some relative velocity, the wavelength of the signal that we observe will be Doppler shifted compared to the emitted signal. This shift in wavelength can be detected using the characteristic emission lines of the source as a reference point. If a source is moving away from us, its wavelength will be shifted towards the red part of the visible spectrum, hence the term redshift. For sources moving

towards us, the light will be blueshifted. The redshift of such a source is then defined as

$$z = \frac{\lambda_{\text{obs}} - \lambda_{\text{em}}}{\lambda_{\text{em}}} = \frac{v}{c} \quad (1)$$

where the second equality comes directly from the nonrelativistic Doppler shift formula. As the shifts in wavelength of more galaxies were measured, it became apparent that the vast majority of them were redshifted, and only a couple were blueshifted. This was an unexpected result at the time since there was no sensible way to explain the fact that celestial objects predominantly move away from rather than towards us in a static Universe. The final blow to the static model came from the data collected by [Hubble \(1929\)](#), who measured the redshifts of galaxies as a function of their radial distance from Earth.

From these observations it became clear that the redshift, and therefore the radial velocity away from us, increases as a function of distance, and does so in an approximately linear manner. In equations, we can write

$$\begin{aligned} z &= \frac{H_0}{c} d \\ v &= H_0 d \end{aligned} \quad (2)$$

where d is the radial distance and $H_0 \approx 67$ (km/s)/Mpc is the constant of proportionality, known as the Hubble constant. Note that the above equations are approximations that are only valid up to linear order, so for small values of d (and z); the more general relations can be derived using General Relativity. Eq. (2) is clearly not consistent with a static Universe, as it implies that everything is moving away from us and that the velocity increases as a function of distance. In fact, it is quite straightforward to show that these results imply that not only is everything moving away from *us*, but that actually everything is moving away from everything else (which has to be the case in order for the Universe to be isotropic and homogeneous). In other words, we live in an expanding Universe.

The fact that redshift relates to distance in this way allows us to use it as an approximate measure of cosmological distances, which as we will see is extremely useful for constructing 3D maps from redshift surveys. Furthermore, since light that is observed from sources that are further away was actually emitted at an earlier time (due to the finite speed of light), we can also use redshift as measurement of time, with $z = 0$ being the present time. Given that distances between celestial objects are increasing, one is naturally led to the conclusion that in the past the Universe must have been a much more compact and dense place. Extrapolating all the way back to the beginning of time leads to the Big Bang model, where all energy and matter is thought to have originated from a singularity about 13.8 billion years ago, which is our current estimate for the age of the Universe.

2.1.2 The early Universe and the CMB

The early Universe was a very dense and hot place. The conditions were so extreme that not even subatomic particles were stable, and as a result photons and baryons were coupled in a hot ionized plasma which was opaque to radiation. As the Universe expanded and thus cooled down, there were three key moments in the early history of the Universe: recombination, photon decoupling, and the last scattering. Recombination refers to the time at which the

temperature had dropped sufficiently for the ionized particles to bond and form neutral atoms. Shortly afterwards came photon decoupling, where the rate at which photons scatter of electrons dropped dramatically due to recombination. This transition allowed photons to move freely and thus marks the moment the Universe became transparent to radiation. Closely related to this is the time of last scattering, which refers to the last time photons scattered off electrons before traveling freely in a now transparent Universe.

These photons carry valuable information about the conditions of the early Universe, and it turns out that we can still detect them today in the form of the cosmic microwave background (CMB) radiation (Penzias and Wilson, 1965). This nearly uniform background radiation very accurately matches the spectrum of an ideal blackbody radiating at the temperature of the Universe at the time of last scattering (cooled down over its expansion), and thus serves as strong evidence of a hot and dense early Universe (Dicke et al., 1965). However, the temperatures for the CMB we detect are not exactly uniform in all directions; there are minor but significant fluctuations. By decomposing the signal into a suitable basis of spherical harmonics, it is found that these fluctuations follow a well-defined structure with peaks in the signal at specific angular separations (Smoot et al., 1992). How can we explain the structure of these fluctuations?

The ionized plasma before recombination was dense enough that acoustic (pressure) waves were able to oscillate in characteristic modes defined by the speed of sound in the medium at that time. At the time of recombination, the sudden change in medium meant that these pressure waves could no longer propagate and were effectively ‘frozen’ in time, leaving their mark in the form of a specific pattern of high and low pressure (and thus density) regions. These density differences correspond to temperature fluctuations, which consequently were also frozen in time and are still visible today in the form of the fluctuations in the CMB, which match the structure predicted by the speed of the sound at the time of recombination. This feature, which is still detectable today, is known as the baryonic acoustic oscillations (BAO) feature and is another key concept in our understanding of the history of the Universe.

2.1.3 The growth of structure

Although the Universe might be homogeneous at sufficiently large scales, when zooming in a little bit more it is clear that the density distribution is far from uniform (see title page image). When studying the large-scale structure of the Universe - by which we mean all structures larger than individual galaxies, such as clusters, superclusters, voids, filaments, etc. - it becomes apparent that galaxy positions are not random but are instead correlated with one another; they are mainly found clustered together, separated by low density voids. What is the origin of the structure of the ‘cosmic web’ we see today? To answer that question we have to study how matter density perturbations have evolved over time since the early Universe. This and the following subsection are largely based on Chapter 7 & 11 from Ryden (2017).

The seeds for the large-scale structure today were sown in the early Universe, and they were able to grow due to the effect of the gravitational force. Quantum fluctuations in the early Universe resulted in small matter density fluctuations that persisted throughout the evolution of the Universe. It is useful to define a dimensionless parameter to describe such

matter density perturbations:

$$\delta(\mathbf{r}, t) \equiv \frac{\rho_m(\mathbf{r}, t) - \bar{\rho}_m(t)}{\bar{\rho}_m(t)} \quad (3)$$

where $\rho_m(\mathbf{r}, t)$ is the matter density as a function of position and time, and $\bar{\rho}_m(t)$ is the average matter density over a sufficiently large region. Over time, regions which are overdense will attract more matter and get even more dense, while underdense regions will ‘lose’ even more matter. If not for pressure, these overdense regions would collapse under gravity on an exponential timescale. Because a pressure gradient does arise, regions can maintain hydrostatic equilibrium, where the outward pressure force balances the inward gravitational force. By the virial theorem, equilibrium is achieved if $2K = -U$, where K and U are the total average kinetic and potential energy of the region. If twice the kinetic energy is more than $-U$, the region will expand in size and *vice versa*. For a region with a specific average density one can then define a length scale, known as the *Jeans length*, which marks the minimum length scale of a perturbation that is needed for regions to collapse under gravity. For perturbations of scales less than the Jeans length there will instead be stable acoustic oscillations.

It is important to note that the Jeans length depends on the equation of state of the medium that you are considering, and in particular that it scales linearly with the speed of sound of that medium. Before the time of decoupling, the speed of sound of the baryon-photon fluid was very large, and consequently the Jeans length was very large. In fact, if one calculates the baryonic Jeans mass (the mass of a sphere with the Jeans length as radius) before decoupling we get $M_J \approx 10^{19} M_\odot$ (Ryden, 2017). This means that only overdense regions with this mass were able to gravitationally collapse and grow in size, which is a very large mass even compared to masses of galaxy clusters at present time and thus acted as a barrier to the growth of structure. After decoupling the baryonic speed of sound, and thus the Jeans length, decreased by a factor $\sim 10^{-5}$, leading to a decrease in the Jeans mass by a factor of $\sim 10^{-15}$. This suddenly allowed density perturbations of much smaller masses to collapse under gravity. The important takeaway here is that baryonic overdense regions were only able to grow significantly in size after decoupling, which marks the start of the growth of structure.

For small density perturbations, such that $|\delta| \ll 1$, the time evolution of matter density perturbations is described by the following differential equation:

$$\ddot{\delta} + 2\frac{\dot{a}}{a}\dot{\delta} - \frac{3}{2}\Omega_m \left(\frac{\dot{a}}{a}\right)^2 \delta = 0 \quad (4)$$

There are a few new parameters here that are important to introduce. Firstly, $a = a(t) = \frac{1}{1+z}$ is the scale factor which describes the scale of the Universe relative to the present, such that $a(0) = 1$. The time derivative of a therefore describes the rate of change in the size of the Universe, which is related to the Hubble parameter by $H = \frac{\dot{a}}{a}$. The parameter Ω_m is a dimensionless measure of the fraction of the critical energy density that is taken up by matter. For a flat Universe the critical energy density is equivalent to the total energy density of all combined components (matter, radiation, etc.).

$$\Omega_m = \frac{\bar{\epsilon}_m}{\epsilon_c} = \bar{\epsilon}_m \frac{8\pi G}{3c^2 H^2} \quad (5)$$

Equation (4) is really useful because it allows us to study how density perturbations evolve over time in different epochs of the Universe. However, it is important to keep in mind that it is only valid for small (linear) perturbations. Because smaller structures collapse before larger ones, small scales tend to have larger perturbations and have entered the nonlinear regime, whereas larger scale perturbations tend to stay smaller and remain linear. For that reason, linear perturbation theory concerns itself mainly with large scale perturbations, otherwise nonlinear corrections are needed. Another useful takeaway from equation (4) is that the time evolution of the perturbations is independent of the spatial position. In other words, we can separate the perturbation into a temporal and a spatial part:

$$\delta(\mathbf{r}, t) = D(t)\Delta(\mathbf{r}) \quad (6)$$

where $D(t)$ is called the *growth factor*, which is a very sought-after quantity in cosmology, and $\Delta(\mathbf{r})$ is an arbitrary function representing the spatial component of $\delta(\mathbf{r}, t)$. The above equation is important because it means that the rate at which density perturbations grow is the same everywhere; it depends only on the growth factor and not on the position. In other words, we can write

$$\delta(\mathbf{r}, t) = \delta(\mathbf{r}, t_i) \frac{D(t)}{D(t_i)} \quad (7)$$

where t_i is some arbitrary initial time. In practice we often work with the logarithmic derivative of the growth factor with respect to the scale factor. This quantity, known as the linear *growth rate*, is defined as

$$f = \frac{d \ln D}{d \ln a} = \frac{a}{D} \frac{dD}{da} \quad (8)$$

Obtaining precise constraints on the growth rate f is the aim of many cosmological studies because it holds valuable information about the expansion history of the Universe.

2.1.4 The Λ CDM model

As discussed above, the baryonic matter perturbations were only able to start growing after decoupling at $z_{\text{dec}} \approx 1090$. From what we know about the growth factor, it turns out that baryonic matter alone cannot account for the growth of structure that is needed to arrive at the large-scale structure that we see today. An additional type of matter, called *dark matter*, is needed to explain the growth that we observe. There are other reasons to suspect the existence of another type of matter that does not interact with light. For example, it was observed that baryonic matter alone cannot account for the high orbital velocities that we find in the spiral arms of galaxies; there must be dark matter halos that make up most of the galaxy mass (Rubin and Ford Jr, 1970). There are many potential candidate particles for such dark matter but their exact nature remains unknown, although there is now substantial evidence that some form of dark matter does exist (see for example Clowe et al. (2006)). The most promising options all fall into the category of *cold* dark matter, meaning that they behaved nonrelativistically at the time they decoupled from the other components of the Universe.

Another key observation that shapes our models is the fact that the expansion of our Universe is accelerating, which was confirmed by measurements of supernovae (Riess et al.,

1998). This would be surprising if matter and radiation were the only components of the Universe, since both act to slow down the expansion. What then could cause this acceleration? It is assumed that there must be another component to our Universe, which we refer to as *dark energy*. The leading candidate for dark energy is the cosmological constant Λ , which has the unique property that its energy density is independent of the scale factor, and that it exerts a negative pressure, which results in the accelerating expansion. The exact nature of dark energy is still very much unknown and is one of the key open questions in cosmology.

Putting this all together we arrive at the Λ CDM model, which is currently the most simple model that still accurately describes several key observations: the CMB, the large-scale structure, and the accelerating expansion of the Universe. It uses the following approximate energy distribution for the different components of our Universe: 68.5% dark energy, 27% dark matter, and 4.5% baryonic matter (Planck Collaboration et al., 2020). Unless stated otherwise these are the values used in any calculations in this thesis. Since the radiation density scales as a^{-4} and the matter density as a^{-3} , we know that the early Universe was radiation dominated, followed by an epoch of matter domination, and that presumably in the future dark energy will dominate. This model sets the stage for any research in the field of cosmology, and with upcoming surveys we expect to be able to provide even better constraints for the many model parameters.

It is important to emphasize that although the distribution of energy across the different components of the Universe is fairly well known, we know relatively little about what the ‘dark’ components consist of. We know some form of dark energy must exist to account for the accelerating expansion, but fundamental theories on what it really is vary widely (Mortonson et al., 2013). Constraining such theories is the aim of many upcoming surveys (for example LSST DESC et al. (2018)). This uncertainty highlights the significance of galaxy redshift surveys because they are able to probe the growth rate and thus the expansion history of the Universe, which gives us insight into the nature of dark energy. The fact that they can do this at low redshifts (late times) is especially important because that is when dark energy dominates; other probes like the CMB can only access high redshift information when dark energy was not significant yet. But how exactly do we extract this valuable information from the night sky? What observational probes do we have available that allow us to constrain our models?

2.2 Observational probes

There are various methods that astronomers and cosmologists use to access all this information observationally. Some of these are already mentioned above, such as the CMB and the BAO feature, the latter of which can act as a *standard ruler*. A standard ruler is a feature of known length, so that when we observe its apparent size in the sky we can infer its distance away from us. Similarly, one can use *standard candles*, which are celestial objects with a known luminosity, to infer cosmological distances by measuring their apparent luminosity. Typical examples of standard candles are Cepheid variable stars or type Ia supernovae (Ryden, 2017). Another promising method of probing the large-scale structure observationally is through weak gravitational lensing, which refers to the smearing out of galaxy images due to light bending slightly on its way to us because of the gravitational effect of nearby masses.

In case we want to use complex multidimensional fields as observational probes, such as

the CMB or the matter density perturbation field, we are generally not so interested in the exact values of these fields at every single point in space and time (nor are we able to predict these), but rather in their overall statistical properties. The most important mathematical tools we use to study these properties are the correlation function and the power spectrum. The next two subsections (2.2.1 and 2.2.2) are largely based on [Dodelson and Schmidt \(2020\)](#) (Chapter 11).

2.2.1 Correlation functions and power spectra

In order to study the statistical properties of the matter density perturbation field (as defined in Eq. (4)), we make use of a *two point auto-correlation function*. In general, a correlation function quantifies the statistical correlation between a number of quantities (fields), as a function of some variable. In our case, that variable is the distance between two points with some value $\delta(\mathbf{r})$. The term ‘two point’ refers to the fact that we are considering the correlation between two quantities, while the ‘auto’ indicates that these quantities are the same, in our case the matter density field. Compare this with cross-correlation functions, which study the correlations between two different fields. Unless stated otherwise, we will simply refer to the two point auto-correlation function as ‘the correlation function’.

In our case, this function measures the excess probability of finding a pair of overdensities separated by a certain distance $|\mathbf{r}_1 - \mathbf{r}_2|$. It is defined as

$$\xi(r) = \xi(|\mathbf{r}_1 - \mathbf{r}_2|) = \langle \delta(\mathbf{r}_1)\delta(\mathbf{r}_2) \rangle \quad (9)$$

where the angular brackets denote an average over all possible realizations of $\delta(\mathbf{r})$ in a given survey volume, for a given value of r . If matter was uniformly distributed over all space, we would have $\xi(r) = 0$ for all values of r , but instead we find that the matter density field is clearly correlated with itself, as can be seen in Figure (1), which shows the galaxy clustering correlation function as a function of r . Due to the gravitational force galaxies tend to cluster together, so we are more likely to find them separated at shorter distances. However, a small but significant peak is also detected at larger separations, and this separation corresponds exactly to the BAO feature and also matches the peak in the CMB fluctuations ([Eisenstein et al., 2005](#)). This should come as no surprise, since the large-scale structure grew from the same acoustic patterns left in the density field upon recombination that also caused the CMB temperature fluctuations.

As mentioned before, the linear perturbation theory that we are using is only valid for sufficiently large scales, since small-scale overdensities will already have grown nonlinear. For that reason it is very useful to have a statistic that easily allows us to separate the small from the large scales, which is why it is often preferred to work with the correlation function in Fourier space. We thus define the matter power spectrum $P_{\delta\delta}(k)$ as the Fourier transform of the correlation function, such that

$$\xi(|\mathbf{r}_1 - \mathbf{r}_2|) = \frac{1}{(2\pi)^3} \int d^3\mathbf{k} P_{\delta\delta}(k) e^{i\mathbf{k}(\mathbf{r}_1 - \mathbf{r}_2)} \quad (10)$$

where $k = \frac{2\pi}{\lambda}$ is the wavenumber of the Fourier mode. We can isolate $P_{\delta\delta}(k)$ by taking the Fourier transform of both sides of the above equation, which, using the definition of Eq. (9),

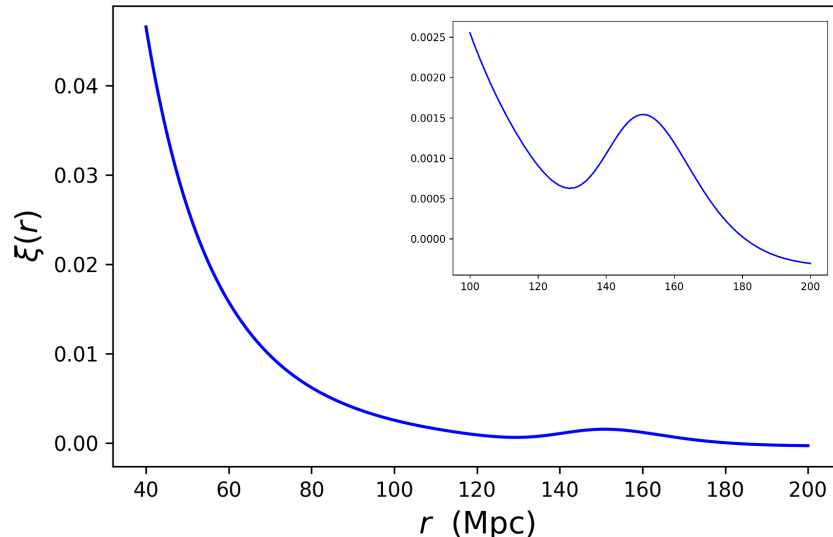


Figure 1: The correlation function of galaxies as a function of their separation in Mpc. As expected the value drops off with increasing distance, but a clear peak is detected around 150 Mpc, which corresponds to the BAO feature. The top right panel is a zoom in on the BAO bump. Figure based on Figure 2 of Eisenstein et al. (2005), but created by author using the Core Cosmology Library at $z = 0$; the exact settings used are discussed in section 3.3.

gives us

$$\langle \delta(\mathbf{k})\delta(\mathbf{k}') \rangle = (2\pi)^3 P_{\delta\delta}(k) \delta_D^3(\mathbf{k} - \mathbf{k}') \quad (11)$$

where δ_D^3 represents the three dimensional Dirac delta function, and $\delta(\mathbf{k})$ is the Fourier transform of the overdensity defined in Eq. (4). For a generic power spectrum between two variables X and Y , we can then write

$$P_{XY}(k) = \frac{1}{(2\pi)^3} \int d^3\mathbf{k}' \langle X(k')Y(k) \rangle \quad (12)$$

The matter power spectrum, often referred to as the linear power spectrum (for linear scales), holds a lot of information. It decomposes the correlations between overdensities into different length scales, defined by their k -mode, for which the value of $P_{\delta\delta}(k)$ indicates the ‘power’, or relative strength, of the correlation at that length scale. This is an extremely useful statistic as it allows us to separate the statistics of the large-scale structure by length scale, and it will be used extensively throughout this thesis. It serves as a powerful tool to constrain our cosmological models by comparing theory to observations, but in practice it is very difficult to measure the matter power spectrum directly. This is complicated further because the majority of the matter is in fact dark matter and cannot be observed directly in the first place. How then do we access this useful statistic? Luckily we can indirectly probe the linear matter power spectrum through other observables which we *can* measure and are related to the matter power spectrum. One such observable is *galaxy clustering*, where we measure the galaxy-galaxy power spectrum to trace the large-scale structure of the Universe.

2.2.2 Redshift space distortions

Measuring the galaxy-galaxy power spectrum, $P_{gg}(k)$, is generally a much easier task because galaxies are relatively easy to observe in the night sky. By measuring the angular positions and redshifts of a large sample of galaxies we can create a 3D map of those galaxies and from there construct a power spectrum. The approximate distances are obtained from the redshifts using the Hubble relation (Eq. (2)). This gives us $P_{gg}(k)$ but in the end what we are after is $P_{\delta\delta}(k)$, so we need to know how the galaxy density field relates to the matter density field. We expect them to be related since galaxies grow out of matter overdensities, but the fields are not equal because the process of galaxy formation is highly complicated and nonlinear. There are two main factors that distort the galaxy density field with respect to the matter one: *bias* and *peculiar velocities*. Bias refers to the fact that the galaxy density field is related to but does not equal the matter density field due to the aforementioned reasons. Typically, a linear bias relation is assumed, which implies that

$$\delta_g(\mathbf{r}, t) = b_g \delta_m(\mathbf{r}, t) \quad (13)$$

where δ_g and δ_m refer to the galaxy and matter density field, respectively, and b_g is the galaxy bias parameter. Note that again the above relation is an approximation that only holds at linear order, *i.e.* on sufficiently large scales. The second distorting factor has to do with the fact that when we use the Hubble relation to convert a galaxy's redshift to a distance, we are implicitly assuming that the galaxy's velocity and thus redshift is only due to the Hubble expansion, whereas in fact galaxies also have peculiar velocities. If these peculiar velocities have a radial component they will affect the redshift and thus the distance we get out of the Hubble relation. What complicates this effect is that peculiar velocities are generally not random but are in fact correlated with the matter density field; galaxies will be attracted to other overdense regions by the gravitational force and thus accumulate a velocity towards it. These effects due to peculiar velocities distort our mapmaking in redshift space and are generally referred to as *redshift-space distortions* (RSDs).

We can get a qualitative intuition for these RSD effects by considering an overdense region surrounded by other galaxies, as depicted in Figure (2). Galaxies that are 'in front' of the overdense region with respect to us will have a peculiar velocity radially away from us, which will increase their redshift compared to the Hubble redshift and therefore cause us to overestimate their distance. For galaxies 'behind' the overdensity the effect is the opposite: their peculiar velocity is directed radially towards us and therefore their redshift is decreased, causing us to underestimate their distance. Peculiar velocities without a radial component do not affect the redshift and therefore cause no distortions. The overall effect is that galaxies are 'squashed' along the line of sight, thereby exaggerating galaxy clustering statistics (Kaiser, 1987).

In order to describe this effect quantitatively, we need to know how the matter velocity field relates to the density field, which we can deduce from the continuity equation. In Fourier space, and keeping only linear terms, we get that

$$\mathbf{v}(\mathbf{k}) = i f a H \frac{\mathbf{k}}{k^2} \delta(\mathbf{k}) \quad (14)$$

where \mathbf{v} from now on refers to the matter peculiar velocity field, and f is the growth rate defined in section 2.1.3. Note that in deriving the above relation we have assumed that

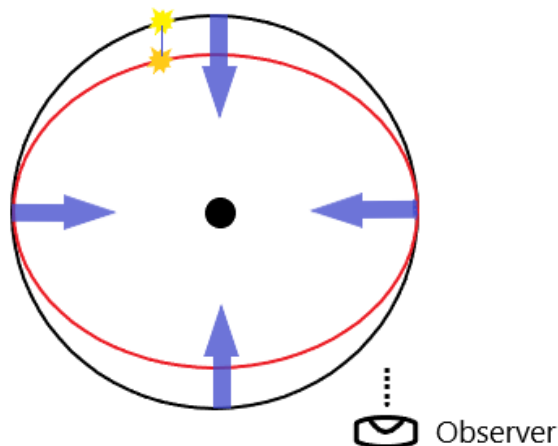


Figure 2: A qualitative intuition of RSDs at linear scales. The figure shows a central overdensity surrounded by other galaxies, whose real space position is shown by the black circle. The RSDs results in a distortion shown by the red ellipse, which ‘squashes’ the galaxy positions together, thereby exaggerating galaxy clustering. Figure based on Figure 11.3 of [Dodelson and Schmidt \(2020\)](#).

peculiar velocities are generally longitudinal, which means they are irrotational (curl-free) in real space and therefore lie along \mathbf{k} in Fourier space. We can then use this result to modify Eq. (13) in order to include RSD effects ([Kaiser, 1987](#)):

$$\delta_g(\mathbf{k}) = (b_g + f\mu^2)\delta_m(\mathbf{k}) \quad (15)$$

where μ is the cosine of the angle between \mathbf{k} and the line of sight. For k -modes perpendicular to the line of sight we thus have $\mu = 0$ and the RSD term vanishes, which makes sense since the distortion only appears due to the radial component of the peculiar velocities. In deriving this equation we implicitly introduced the distant-observer approximation, which assumes that the radial direction of galaxies in your sample is roughly fixed at the line of sight for sufficiently small angular scales. From the above relation and Eq. (12) it immediately follows that

$$P_{gg}(k, \mu) = (b_g + f\mu^2)^2 P_{\delta\delta}(k) \quad (16)$$

which is the expression we were after. We find that both b_g and f contribute to amplifying the galaxy power spectrum with respect to the matter spectrum, but because f is multiplied by μ^2 we can isolate their individual effects by varying μ as well as k . In practice this is often done through a decomposition into multipoles (see for example [Hamilton \(1992\)](#)), which will be discussed in more detail later. The important takeaway is that we are able to constrain the linear growth rate f by measuring the galaxy clustering power spectrum, which is often the aim of cosmological studies (see [Gil-Marín et al. \(2016\)](#), for example). In this way RSDs act as a powerful observational probe to constrain our cosmological model.

2.3 Intrinsic alignments

As galaxy redshift surveys improve their precision and increase their survey volume, we will be able to get much more precise constraints on our model parameters (Richard et al., 2019). At the same time, a higher precision demands a more careful consideration of potential sources of error that previously were neglected. The focus of this thesis is on one of these potential sources of error, namely the intrinsic alignments of galaxies with the local gravitational tidal field, where galaxy intrinsic alignments refers to the correlations between the shapes, orientations, and positions of galaxies (Martens et al., 2018). As it turns out, such alignments can significantly distort galaxy clustering statistics in an anisotropic manner and thereby lead to misleading constraints on the growth rate (Hirata, 2009). In this subsection, the underlying theory of intrinsic alignments is discussed, as well their effect on galaxy redshift surveys.

2.3.1 Linear alignment model

The linear alignment model describes how galaxies align with gravitational tidal fields and provides a framework to quantify intrinsic alignment (IA) effects. It was first proposed by Catelan et al. (2001), but has since then been used extensively in other studies such as Singh et al. (2015), Okumura et al. (2019), Kurita et al. (2020), and van Gemenen and Chisari (2020), which are used in the writing of this subsection.

We start by defining the galaxy intrinsic ellipticity, which is given by

$$\gamma^I = \frac{1 - (b/a)^2}{1 + (b/a)^2} \quad (17)$$

where b and a are the minor and major axis of the projected shape, respectively (Okumura et al., 2019). This ellipticity is typically decomposed into two components given by

$$\gamma_{(+,\times)}^I = \gamma^I (\cos 2\theta, \sin 2\theta) \quad (18)$$

where θ is the angle between the galaxy's position and the reference axis. The observed shape in surveys is actually the sum of multiple components, namely a galaxy's random shape, its intrinsic shape, and a shape distortion due to weak lensing. Since in this thesis we are only interested in the intrinsic shapes, we will from here on drop the superscript I and refer to the intrinsic shape as $\gamma_{(+,\times)}$.

The basic idea behind the linear alignment (LA) model is that a galaxy's shape will trace the gravitational tidal field. If during its formation a galaxy is in a gravitational tidal field due to some nearby overdense region, the gravitational force it feels on the side closest to the overdense region will be slightly stronger than the force it feels on the farther side. The overall effect is a stretching along the gradient of the gravitational field, as depicted in Figure (3); note that this is roughly the same mechanism that drives ocean tidal motion on Earth.

To describe this effect quantitatively, the LA model assumes that, to first order, the intrinsic ellipticity of a galaxy follows a linear relation with the primordial gravitational potential Ψ_P (Okumura et al., 2019),

$$\gamma_{(+,\times)}(\mathbf{r}) = -\frac{C_1}{4\pi G} (\nabla_x^2 - \nabla_y^2, 2\nabla_x \nabla_y) S[\Psi_P(\mathbf{r})] \quad (19)$$

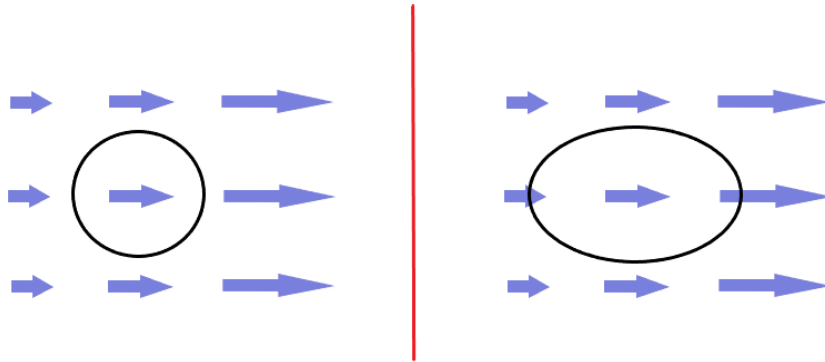


Figure 3: A schematic illustration of the basic idea behind the linear alignment model. The blue arrows represent the local tidal field around a galaxy (black circle). Over time, a galaxy that was initially symmetric in shape (left image) will be stretched along the gradient of the local gravitational field (right image). Figure based on Figure 1 of [Catelan et al. \(2001\)](#).

where C_1 is a parameter that describes the alignment strength, G is the Newtonian gravitational constant, and S is a smoothing filter that acts to smooth out fluctuations in the gravitational potential at halo scales. For the large scales we are considering, this filter can be neglected. The x and y axes are on the plane of the sky, leaving the z axis to be the line of sight direction. The parameter C_1 is generally observed to be positive, which indicates that galaxies tend to align along the stretching axis of the tidal field ([Singh et al., 2015](#)). We now want to relate the gravitational potential to the matter overdensity field. We can do this through the Poisson equation, which, in Fourier space, is given by

$$\Psi_P(\mathbf{k}) = -4\pi G \frac{\bar{\rho}_m(z)a^3}{D(z)} k^{-2} \delta(\mathbf{k}) \quad (20)$$

where $\bar{\rho}_m(z)$ and $D(z)$ are the redshift dependent average matter density and growth factor, respectively, and a is the scale factor. We can then take the Fourier transform of Eq. (19) and plug in Eq. (20) to find

$$\gamma_{(+,\times)}(\mathbf{k}) = -\frac{C_1 \bar{\rho}_m(z) a^3}{D(z)} \frac{(k_x^2 - k_y^2, 2k_x k_y)}{k^2} \delta(\mathbf{k}) = -\tilde{C}_1(z) \frac{(k_x^2 - k_y^2, 2k_x k_y)}{k^2} \delta(\mathbf{k}) \quad (21)$$

where we have used the fact that the ∇ operator in real space corresponds to a $i\mathbf{k}$ in Fourier space. Note that we absorbed the prefactors into a new parameter for the alignment strength, given by

$$\tilde{C}_1(z) = \frac{C_1 \rho_{\text{crit}} \Omega_{m,0}}{D(z)} = \frac{C_1 \rho_{\text{crit}}}{D(z)} \frac{\rho_{m,0}}{\rho_{\text{crit}}} = \frac{C_1 \bar{\rho}_m(z) a^3}{D(z)} \quad (22)$$

2.3.2 Alignment power spectra

With the LA model we have a way of relating the intrinsic ellipticity of galaxies to the matter density field, so the next step is to translate Eq. (21) into a power spectrum that is observable by our surveys. In practice, a more useful decomposition of the ellipticity turns out to be into

E - and B -modes, where the former are curl-free and the latter divergence-free modes. These modes can be calculated from the $+$ and \times modes that we defined earlier in the following way:

$$\begin{aligned}\gamma_E(\mathbf{k}) &= \gamma_+(\mathbf{k}) \cos 2\phi + \gamma_\times(\mathbf{k}) \sin 2\phi \\ \gamma_B(\mathbf{k}) &= -\gamma_+(\mathbf{k}) \sin 2\phi + \gamma_\times(\mathbf{k}) \cos 2\phi\end{aligned}\tag{23}$$

where $\phi = \tan^{-1}\left(\frac{k_x}{k_y}\right)$. This is a useful decomposition because in the LA model all B -modes vanish at first order, so from here on we can restrict our analysis to the E -modes only (Blazek et al., 2011). From basic trigonometry, it follows that

$$\begin{aligned}\cos 2\phi &= 2 \cos^2 \phi - 1 = 2 \left(\frac{k_x^2}{k_x^2 + k_y^2} \right) - 1 = \frac{k_x^2 - k_y^2}{k_x^2 + k_y^2} \\ \sin 2\phi &= 2 \sin \phi \cos \phi = 2 \left(\frac{k_x k_y}{k_x^2 + k_y^2} \right)\end{aligned}\tag{24}$$

Using Eq. (21) and the above relations, we can then write the E -mode as

$$\gamma_E(\mathbf{k}) = -\frac{\tilde{C}_1}{k^2} \left(\frac{(k_x^2 - k_y^2)^2 + 4k_x^2 k_y^2}{k_x^2 + k_y^2} \right) \delta(\mathbf{k}) = -\tilde{C}_1 \frac{k_x^2 + k_y^2}{k^2} \delta(\mathbf{k})\tag{25}$$

Using the fact that $k^2 = k_x^2 + k_y^2 + k_z^2$ and $\mu = \frac{k_z}{k}$ as defined earlier, we finally arrive at

$$\gamma_E(\mathbf{k}) = -\tilde{C}_1(1 - \mu^2)\delta(\mathbf{k})\tag{26}$$

We are now able to define two new observable power spectra using Eq. (12) and the equation above. Firstly, there is the power spectrum of the galaxy shape E -mode auto-correlation,

$$P_{EE}(k, \mu) = \left[\tilde{C}_1(1 - \mu^2) \right]^2 P_{\delta\delta}(k)\tag{27}$$

but we can also define the cross power spectrum between the galaxy density field and the E -modes, which is given by

$$P_{gE}(k, \mu) = -\tilde{C}_1(1 - \mu^2)(b_g + f\mu^2)P_{\delta\delta}(k)\tag{28}$$

These power spectra can be observed and compared to theoretical models to constrain the model parameters, as is done by Singh et al. (2015) and Taruya and Okumura (2020), for example.

2.3.3 Selection effects

The intrinsic alignments of galaxies can cause systemic errors to RSD measurements and thereby contaminate our constraints on the linear growth rate f (Hirata, 2009). For that to happen, two conditions must be met: 1) galaxy orientations cannot be random, they must be correlated with the matter density field and 2) there must be a selection effect in spectroscopic surveys that depends on the galaxy orientation with respect to the line of sight. The first

condition is met by the linear alignment model and the various studies that confirm its validity such as [Blazek et al. \(2011\)](#) and [Singh et al. \(2015\)](#). The second condition, the selection effect, can be explained as follows: galaxies which are aligned along the line of sight have a smaller projected area on the sky than galaxies which are aligned perpendicularly. For a given number of stars, the smaller area will appear brighter and is thus more likely to be observed by spectroscopic surveys. In this way, galaxies aligned along the line of sight have a higher probability of being observed than perpendicularly aligned galaxies. Combined with non-random orientations, this anisotropically distorts galaxy clustering statistics ([Martens et al., 2018](#)).

Consider the left panel of Figure (4), where a survey is observing a patch of sky where the galaxies are predominantly aligned along the line of sight. The few galaxies that are aligned perpendicularly are less likely to be observed, which is shown by the crossed out galaxies. The overall effect is that the perpendicular k -modes for the galaxy clustering power spectrum will be amplified, since low density region between clusters will seem even emptier. Another case is shown in the right panel, where most galaxies are aligned perpendicularly. In this case the signal of a parallel k -mode of the clustering power spectrum will be dampened due to the selection effect. The overall effect is an anisotropic distortion in the galaxy clustering power spectrum that is hard to separate from RSDs. In [Martens et al. \(2018\)](#) they split their galaxy sample by their alignments and indeed find significant differences in the clustering statistics for both cases.

This effect is described quantitatively by [Hirata \(2009\)](#), whose work is followed here. If we denote the contribution of this selection effect on the galaxy density field by $\epsilon(\hat{\mathbf{n}}|\mathbf{r})$, then to linear order we can write

$$\delta_g(\mathbf{k}) = (b_g + f\mu^2)\delta_m(\mathbf{k}) + \epsilon(\hat{\mathbf{n}}|\mathbf{k}) \quad (29)$$

If we assume a linear alignment model, then this contribution depends on the large-scale tidal field. Specifically, we find that

$$\epsilon(\hat{\mathbf{n}}|\mathbf{r}) = A \left[\left(\nabla_i \nabla_j \nabla^{-2} - \frac{1}{3} \delta_{ij} \right) \delta_m(\mathbf{r}) \right] \hat{n}_i \hat{n}_j \quad (30)$$

where the term in square brackets represents the dimensionless tidal field, and A parametrizes the strength of the overall intrinsic alignment effect on RSD measurements, which includes *both* the strength of intrinsic alignments and the observational selection effect. Eq. (29) leads to a new expression for the galaxy clustering power spectrum of the following form ([Hirata, 2009](#)):

$$P_{gg}(k, \mu) = \left[b_g - \frac{A}{3} + (f + A)\mu^2 \right]^2 P_{\delta\delta}(k) \quad (31)$$

The above equation is extremely helpful, because it allows us to reduce the effect of intrinsic alignments on RSDs to a single parameter, A . It is important to note that the functional form of P_{gg} has remained the same, in particular its μ -dependence. Effectively, the usual RSD parameters b_g and f are shifted such that $b_g \rightarrow b_g - A/3$ and $f \rightarrow f + A$. What this means is that when we use RSDs to measure f , we should interpret this as a measurement of $f + A$. [Hirata \(2009\)](#) estimates that this contamination of our measurements of the growth rate could lead to errors up to 10% on f , which is quite significant. What complicates the

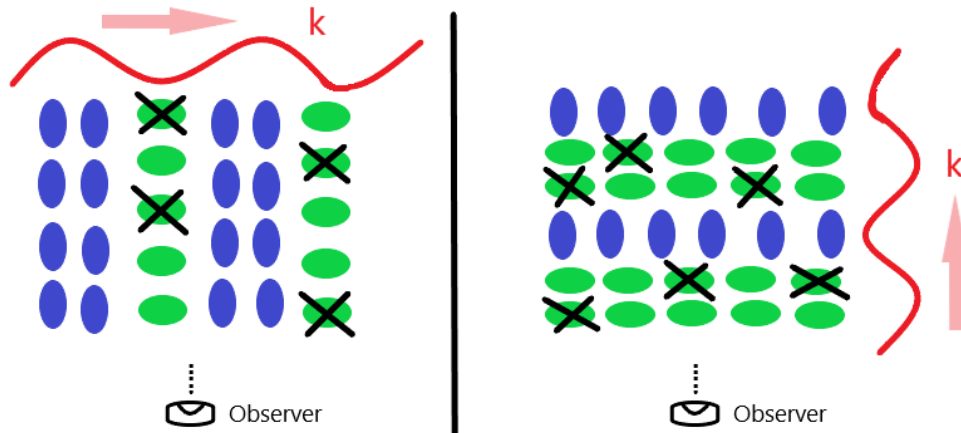


Figure 4: An exaggerated illustration demonstrating the anisotropic selection effect due to intrinsic alignments. Perpendicularly aligned galaxies are less likely to be observed, which is represented by the crossed out galaxies. In this figure, this results in an amplification of the clustering signal for perpendicular k -modes (left panel), and a decrease in the clustering signal for parallel k -modes (right panel). Figure based on Figure 1 of [Martens et al. \(2018\)](#).

issue is that the usual method of disentangling the effects of b_g and f through the different μ -dependence will not work in this case to isolate the effect of A due to the functional form of Eq. (31). There is a degeneracy that can only be broken using additional observables concerning intrinsic alignment effects.

2.3.4 Relationship between A and \tilde{C}_1

If we want to break the degeneracy between f and A using intrinsic alignment statistics such as P_{EE} or P_{gE} , we first have to establish a relationship between the different parameters that are used to quantify the alignment strength, in particular A and \tilde{C}_1 . We know that \tilde{C}_1 describes the alignment strength in the LA model, while A describes the strength of intrinsic alignment effects on RSD measurements, which is a combination of the strength of intrinsic alignments in general *and* the observational selection effect described in the previous subsection. Since the theoretical framework underlying Eq. (30) is also the LA model, it is reasonable to suspect that A depends on \tilde{C}_1 in some way.

In order to find the relationship between these parameters, we have to decompose A into its two contributions: one for the intrinsic alignment strength and one for the orientation-dependent selection effect. This decomposition is done in [Hirata \(2009\)](#) and [Martens et al. \(2018\)](#); we will generally follow [Martens et al. \(2018\)](#). We can then write

$$A = 2(\eta\chi)_{\text{eff}}B \quad (32)$$

where B represents the intrinsic alignment strength and $(\eta\chi)_{\text{eff}}$ the orientation-dependent selection effect. We can interpret $(\eta\chi)_{\text{eff}}$ as the change in the number of observed galaxies with respect to a change in the radial orientation of those galaxies; it describes how sensitive the selection of galaxies is to their orientation.

The individual parameters η and χ come from the original work by [Hirata \(2009\)](#), where η represents the slope of the luminosity function and χ the survey-specific method of computing

fluxes. In this thesis we are not concerned with these specifics and will continue working with $(\eta\chi)_{\text{eff}}$, which represents the overall orientation-dependent selection effect. Eq. (32) confirms our earlier intuition that intrinsic alignment effects will only distort RSD measurements ($A \neq 0$) if we have non-random alignments ($B \neq 0$) and an orientation-dependent selection effect ($(\eta\chi)_{\text{eff}} \neq 0$) (Martens et al., 2018).

The parameters \tilde{C}_1 and B thus represent the same physical thing, namely the strength of intrinsic alignments in the LA model. These parameters should therefore be closely related, and in Martens et al. (2018) they find that¹

$$B = -1.74 \frac{C_1 \rho_{\text{crit}} \Omega_{m,0}}{D(z)} = -1.74 \tilde{C}_1 \quad (33)$$

Using the above relation we can then finally rewrite A in terms of \tilde{C}_1 :

$$A = 2(\eta\chi)_{\text{eff}}(-1.74\tilde{C}_1) = -3.48(\eta\chi)_{\text{eff}}\tilde{C}_1 = R\tilde{C}_1 \quad (34)$$

where for notational convenience we have introduced $R = -3.48(\eta\chi)_{\text{eff}}$. Eq. (34) is powerful because it allows us to use intrinsic alignment statistics to mitigate the selection effect, as will be described below.

3 Method

Based on the previous section, we now have three power spectra which describe the phenomena we are interested in:

$$P_{gg}(k, \mu) = \left[b_g - \frac{R\tilde{C}_1}{3} + (f + R\tilde{C}_1)\mu^2 \right]^2 P_{\delta\delta}(k) \quad (35)$$

$$P_{EE}(k, \mu) = \left[\tilde{C}_1(1 - \mu^2) \right]^2 P_{\delta\delta}(k) \quad (36)$$

$$P_{gE}(k, \mu) = -\tilde{C}_1(1 - \mu^2)(b_g + f\mu^2)P_{\delta\delta}(k) \quad (37)$$

Now that we have discussed in detail the theoretical framework underlying the effect of galaxy intrinsic alignments on RSD measurements, we are ready to delve into the main method that will be used in this thesis to try and mitigate the selection effect. A Fisher forecast is used to predict how well we can constrain the model parameters (b_g , f , and \tilde{C}_1) using some combination of observables based on the equations above. Before exploring the Fisher forecasting formalism, it is important to note that the above equations are *not* what is directly observed because we have not taken into account the μ -dependence. As mentioned briefly before, this is typically handled by decomposing the μ -dependent power spectra into various μ -independent multipoles by expanding them into a basis of Legendre polynomials; see for example Hamilton (1992), Okumura et al. (2020), Gil-Marín et al. (2016), Kurita et al. (2020), or Kobayashi et al. (2020).

¹This relation is found by comparing the work of Hirata (2009) and Singh et al. (2015). In the original Singh et al. (2015) paper (and in others such as Joachimi et al. (2011)) they chose to fix the value of $C_1 \rho_{\text{crit}}$ and introduce a new free parameter, A_I , to represent the alignment strength. Since we are not adopting this choice of fixing C_1 , there is no need to introduce A_I ; this is why it has been omitted in this equation.

3.1 Multipole expansion

The basic idea behind the multipole expansion is that we can isolate the μ -dependence of the power spectra by expanding them into a basis of Legendre polynomials as a function of μ , since these polynomials form a complete and orthogonal set of functions. We can then write that for a general power spectrum P_{XY} ,

$$P_{XY}(k, \mu) = \sum_{l=0}^{\infty} P_{XY}^l(k) \mathcal{L}_l(\mu) \quad (38)$$

where $\mathcal{L}_l(\mu)$ is the l -th order Legendre polynomial. Each multipole moment is then given by:

$$P_{XY}^l(k) = \frac{2l+1}{2} \int_{-1}^1 d\mu P_{XY}(k, \mu) \mathcal{L}_l(\mu) \quad (39)$$

Note that power spectra with an even μ -dependence will only have even-order nonzero multipole moments and vice versa, and that a power spectrum will only have nonzero multipole moments up to the order of its μ -dependence. It can be easily verified that for P_{gg} the only nonzero moments are the monopole ($l = 0$), the quadrupole ($l = 2$), and the hexadecapole ($l = 4$). The most signal is typically contained in the lowest order poles, and in fact the hexadecapole contains such low signal that it is often neglected; we will do the same in this thesis (Blake et al., 2018). For P_{EE} and P_{gE} we will work only with their lowest order nonzero pole, which is the monopole moment. Using Eq. (39) we can calculate the multipole moments of interest:

$$P_{gg}^{(0)}(k) = \left[(b_g - \frac{1}{3}R\tilde{C}_1)^2 + \frac{2}{3}(b_g - \frac{1}{3}R\tilde{C}_1)(f + R\tilde{C}_1) + \frac{1}{5}(f + R\tilde{C}_1) \right] P_{\delta\delta}(k) \quad (40)$$

$$P_{gg}^{(2)}(k) = \left[\frac{4}{3}(b_g - \frac{1}{3}R\tilde{C}_1)(f + R\tilde{C}_1) + \frac{4}{7}(f + R\tilde{C}_1)^2 \right] P_{\delta\delta}(k) \quad (41)$$

$$P_{EE}^{(0)}(k) = \frac{8}{15}\tilde{C}_1^2 P_{\delta\delta}(k) \quad (42)$$

$$P_{gE}^{(0)}(k) = -\tilde{C}_1 \left[\frac{2}{3}(b_g - \frac{1}{3}R\tilde{C}_1) + \frac{2}{15}(f + R\tilde{C}_1) \right] P_{\delta\delta}(k) \quad (43)$$

The multipole moments above are well observable by spectroscopic surveys and are therefore the observables used in the Fisher forecast (Kobayashi et al., 2020). Note again that if intrinsic alignments did not distort RSD measurements ($A = R\tilde{C}_1 = 0$), Eqs. (40 & 41) would be sufficient to constrain both b_g and f , which is what is typically done (see Hamilton (1992) or Gil-Marín et al. (2016)). However, since \tilde{C}_1 now shows up in these expressions as well, we need additional observables (either Eq. (42) or (43)) to break the degeneracy.

3.2 Fisher forecast

Although it is relatively straightforward to *qualitatively* describe how we could account for the contamination of RSD measurements due to intrinsic alignments by including additional

observables, it would be much more useful if we could quantify this idea. One method of doing this is through the Fisher formalism, which can be used to predict how well model parameters can be constrained given a set of observables. This forecasting can be done without using actual survey data and can be helpful in the process of experimental design; if we know which combinations of observables will provide the best constraints we can design our surveys in line with this knowledge. The following subsection is largely based on Chapter 14 of [Dodelson and Schmidt \(2020\)](#).

3.2.1 Fisher formalism

The Fisher formalism derives from the *likelihood function*, which gives us “the probability that an experiment yields the observed data given a theory” ([Dodelson and Schmidt, 2020](#)). We could write that

$$L(\{d\}|\{m, \sigma_m\}) = P(\{d\}|\{m, \sigma_m\}) \quad (44)$$

where L is the likelihood function, $\{d\}$ the data set and $\{m, \sigma_m\}$ the set of model parameters used in the model and their uncertainties. The likelihood function therefore indeed gives us the probability of a certain set of data given a set of model parameters. Often a Gaussian likelihood is assumed, in which case one could easily calculate this probability explicitly. Although this is useful, in general we are after the opposite relation between data and theory, namely the *posterior*. This gives us how likely a theory (and its set of model parameters) is given some observed data. The two are related by Bayes’ theorem:

$$P_{\text{posterior}}(\{m, \sigma_m\}|\{d\}) \propto L(\{d\}|\{m, \sigma_m\}) P_{\text{prior}}(\{m, \sigma_m\}) \quad (45)$$

where P_{prior} is the prior probability, which holds any prior information (constraints) we might have on our model parameters.

If we assume some fiducial (best-fit) model parameters, then by definition these will be the parameter values for which the observed data is most likely. In other words, the likelihood function has a local maximum at these fiducial values. What we are interested in is the curvature of this maximum, which informs us how rapidly the likelihood changes as we move away from the fiducial values. If the likelihood reacts very sensitively to a change in a parameter, then the error on the parameter will be small; even a minor deviation makes the data significantly less likely. If on the other hand the likelihood does not change much when we change a parameter, the error on that parameter will be large; the likelihood is ‘indifferent’ to a change in that parameter. The curvature of the likelihood function is encoded in its second derivative, and in general we can write the *Fisher information value* as

$$F_{ij} \equiv - \left\langle \frac{\partial^2 \ln L}{\partial \theta_i \partial \theta_j} \right\rangle \quad (46)$$

where θ_i are the parameter(s) of interest. We take the natural logarithm of L because this is convenient when working with Gaussian likelihoods.

For a given set of parameters $\{\theta_i\}$, we then obtain what is called the *Fisher matrix*, which is a symmetric square matrix with the number of model parameters as its length, and elements defined by the equation above. The inverse of the Fisher matrix then directly gives

us the covariance matrix of the model parameters, from which we can obtain the best possible constraints on the individual parameters given our model and observables.

There are a couple of ways in which we could slightly modify the Fisher formalism. If we would want to add a prior constraint to one of the model parameters, we could do this by adding $\sigma_{\theta_i}^{-2}$ to the appropriate diagonal element of the Fisher matrix, where σ_{θ_i} is the prior constraint on the parameter θ_i (Coe, 2009). Furthermore, since we are often not interested in all the free parameters we can choose to *marginalize* over some by integrating over their range of possible values. In practice this is done by defining an appropriate submatrix of F^{-1} (Schmidt et al., 2015). We can marginalize over all but one parameter by selecting only the appropriate diagonal element of the covariance matrix. The square root of this element then gives the constraint on that parameter having marginalized over all others. If we want to marginalize over all but two parameters, we can define an appropriate 2x2 submatrix of F^{-1} . This will give us the individual constraints on the parameters as well as their covariance, from which we can construct a 2D confidence ellipse to represent the constraints visually.

3.2.2 Fisher matrix for cosmological observables

The above description is quite general, but it can be made specific for cosmological observables. If we assume a Gaussian likelihood function, the Fisher matrix for cosmological observables is given by (Taruya and Okumura, 2020):

$$F_{ij} = \frac{V_{\text{survey}}}{4\pi^2} \int_{k_{\text{min}}}^{k_{\text{max}}} k^2 dk \int_{-1}^1 d\mu \sum_{a,b} \frac{\partial P_a(k, \mu)}{\partial \theta_i} [\text{cov}^{-1}]_{ab} \frac{\partial P_b(k, \mu)}{\partial \theta_j} \quad (47)$$

where V_{survey} is the volume of the survey, and the sum over a and b indicates a sum over all the observables we are considering in our analysis. The matrix ‘cov’ is the covariance matrix of the observables. For each Fisher matrix element, we thus sum over all observables as well as all possible k - and μ -values, while multiplying by the appropriate element of the inverse of the covariance matrix of the observables. In this way, a large covariance on an observable would lead to a smaller Fisher value, and ultimately a larger error on our parameters. If we assume Gaussian covariances, we can write the covariance between two generic power spectra P_{XY} and P_{WZ} as (Duncan et al., 2013)

$$\text{cov}[P_{XY}, P_{WZ}] = P_{XW}P_{YZ} + P_{XZ}P_{YW} \quad (48)$$

From the above definition one can construct the covariance matrix for the power spectra we are interested in, namely P_{gg} , P_{EE} , and P_{gE} , as given by Taruya and Okumura (2020):

$$\text{cov}_{ab} = \begin{bmatrix} 2(\tilde{P}_{gg})^2 & 2(P_{gE})^2 & 2\tilde{P}_{gg}P_{gE} \\ 2(P_{gE})^2 & 2(\tilde{P}_{EE})^2 & 2\tilde{P}_{EE}P_{gE} \\ 2\tilde{P}_{gg}P_{gE} & 2\tilde{P}_{EE}P_{gE} & \tilde{P}_{gg}\tilde{P}_{EE} + (P_{gE})^2 \end{bmatrix} \quad (49)$$

where the power spectra with a tilde represent the power spectrum plus a shot noise term. Specifically, we have that $\tilde{P}_{gg} = P_{gg} + 1/n_{\text{gal}}$ and $\tilde{P}_{EE} = P_{EE} + \sigma_\gamma^2/n_{\text{gal}}$, where n_{gal} is the

average number density of galaxies, and σ_γ is the shape noise which quantifies the intrinsic dispersion of galaxy shapes.

Each element of the above matrix is actually divided by the number of independent Fourier modes in a given survey volume, which is given by $N_k = 4\pi k^2 dk / (2\pi/L)^3 = V_{\text{survey}} k^2 dk / 2\pi^2$, where the last equality holds because $V_{\text{survey}} = L^3$, with L the side length of the survey volume (Kurita et al., 2020). This is the origin of the prefactor in Eq. (47), which is why it has been omitted in the covariance matrix². We see that the covariances of the power spectra are generally proportional to the power spectra themselves with an added shot/shape noise term due to instrumental or astrophysical sources. The multiplication by N_k^{-1} highlights the fact that there is an irreducible statistical error due to the limited number of Fourier modes that we can sample in a given volume. This error scales as k^{-2} because for large k -modes (small scales in real space) there are many modes to sample, whereas for small k -modes (large scales) there are much fewer modes. This contribution to the covariance is known as *cosmic variance*.

In practice however, as discussed in section 3.1, we do not work with the power spectra directly but with their multipole moments, in our case Eq. (40-43). The covariances must also be transformed to their appropriate multipole moment, which can be done using (Kurita et al., 2020):

$$\text{cov}^{\text{multipole}}[P_{XY}^l, P_{WZ}^{l'}] = \frac{2l+1}{2} \frac{2l'+1}{2} \int_{-1}^1 d\mu \mathcal{L}_l(\mu) \mathcal{L}_{l'}(\mu) \text{cov}[P_{XY}, P_{WZ}] \quad (50)$$

where a factor of $2/N_k$ has been omitted because it is already in the expression for the Fisher matrix. Note that we have an extra factor of $1/2$ compared to Kurita et al. (2020) because they use $1/N_k$ instead of $2/N_k$. This is done so that we get the same prefactor as Taruya and Okumura (2020) in the Fisher matrix expression, which for the multipole case can then be written as

$$F_{ij}^{\text{multipole}} = \frac{V_{\text{survey}}}{4\pi^2} \int_{k_{\text{min}}}^{k_{\text{max}}} k^2 dk \sum_{a,b} \sum_{l,l'} \frac{\partial P_a^l(k)}{\partial \theta_i} [\text{cov}^{-1}]_{ab, ll'}^{\text{multipole}} \frac{\partial P_b^{l'}(k)}{\partial \theta_j} \quad (51)$$

where the integration over μ has been absorbed into the multipole expressions. Note that sum over all observables now refers to the power spectra and their multipole moments, *i.e.* the P_{gg} monopole and quadrupole act as different observables. In our case, the full set of observables is given by Eq. (40-43), and the free parameters are given by $\{\theta_i\} = \{b_g, f, \tilde{C}_1\}$. Using the above expression, one can compute the Fisher matrix for any combination of observables and free parameters.

3.3 Fiducial model

The survey data used in the results that follow is summarized in Table I. It is based on van Gemenen and Chisari (2020), where a combination of 4MOST and LSST galaxy surveys was used. The 4MOST Cosmology Redshift Survey is a spectroscopic survey that will provide detailed measurements of galaxy redshifts and clustering (Richard et al., 2019). The

²The prefactor in Eq. (47) is actually $N_k/2$; we will adjust for this in the multipole formalism.

	$\langle z \rangle$	$n_{\text{gal}}(\text{Mpc}^{-3})$	$V_{\text{survey}}(\text{Mpc}^{-3})$	\tilde{C}_1
4MOST + LSST	0.55	2.9×10^{-4}	1.02×10^{10}	0.026

Table I: The survey data and parameter values used for the Fisher forecast, based on [van Gemenen and Chisari \(2020\)](#).

advantage of spectroscopic surveys is that they are able to achieve a very high precision on redshift data using spectroscopic analysis, but they are unable to accurately detect galaxy shapes. For this purpose photometric surveys such as the LSST are more appropriate, which can measure shape statistics of many galaxies at the cost of lower redshift precision ([Ivezić et al., 2019](#)). To get both accurate redshift and shape data we combine information from both surveys in this thesis.

The fiducial values assumed for this research are as follows. The values for η and χ are based on [Hirata \(2009\)](#); we will use $\eta = 4.0$ and $\chi = 0.06$, which implies $(\eta\chi)_{\text{eff}} = 0.24$. We use $\sigma_\gamma = 0.3$ from [Schmidt et al. \(2015\)](#). For the minimum and maximum k -mode, we use $k_{\text{min}} = 2\pi/V_{\text{survey}}^{1/3} \text{Mpc}^{-1}$ as set by the survey volume and $k_{\text{max}} = \{0.1, 0.5, 1.0\} \text{Mpc}^{-1}$ to stay safely in the linear regime. We vary the value of k_{max} to investigate how the results depend on the scales included in the analysis. All other standard cosmological parameters are computed using the latest version (v2.2.0) of the Core Cosmology Library³ (CCL) ([Chisari et al., 2019](#)). Most importantly, we will use $b_g = 1.7$ and $f \approx 0.777$ ([van Gemenen and Chisari, 2020](#)). The cosmological model settings used for CCL are as follows:

cosmo = ccl.Cosmology(Omega_c = 0.27, Omega_b = 0.045, h = 0.67, A_s = 2.1e-9, n_s = 0.96)

4 Results

Having discussed the methods used in this thesis, we can now present the results obtained by evaluating Eq. (51) for different combinations of observables and free parameters. We will first explore the ‘regular’ case where intrinsic alignments are assumed not to affect RSD measurements, and then see how we can mitigate the selection effect by adding in additional observables. In all ellipse plots that follow in this section the confidence intervals shown are 68.3%, 95.4%, and 99.7%; they are calculated using the formalism described in [Coe \(2009\)](#). Although the errors are calculated for different values of k_{max} , all ellipse plots shown are only for the case where $k_{\text{max}} = 1.0 \text{Mpc}^{-1}$. The results are summarized in Table II.

4.1 Without selection effect

We will first explore the base case, where we assume that there is no selection effect that contaminates our RSD measurements. This means that we can set $R \propto (\eta\chi)_{\text{eff}} = 0$, which implies that the multipole moments of P_{gg} no longer depend on \tilde{C}_1 but only on b_g and f . This is what is implicitly assumed by most RSD surveys, where the effect of intrinsic alignments

³<https://github.com/LSSTDESC/CCL>

Scenario	k_{\max} (Mpc $^{-1}$)	$\delta b_g/b_g$	$\delta f/f$	$\delta \tilde{C}_1/\tilde{C}_1$
$P_{gg}^{(0)}, P_{gg}^{(2)}$ (no IA)	0.1	0.00308	0.0172	-
	0.5	0.000652	0.00322	-
	1.0	0.000543	0.00258	-
$P_{gg}^{(0)}, P_{gg}^{(2)}$ (prior on \tilde{C}_1)	0.1	0.00312	0.0175	0.109
	0.5	0.000800	0.00443	0.109
	1.0	0.000713	0.00399	0.109
$P_{gg}^{(0)}, P_{gg}^{(2)}, P_{EE}^{(0)}$	0.1	0.00312	0.0175	0.119
	0.5	0.000755	0.00408	0.0901
	1.0	0.000659	0.00358	0.0883
$P_{gg}^{(0)}, P_{gg}^{(2)}, P_{gE}^{(0)}$	0.1	0.00308	0.0172	0.0257
	0.5	0.000653	0.00323	0.0113
	1.0	0.000544	0.00260	0.0103

Table II: The results of the Fisher forecast for the various scenarios and different values of k_{\max} . The ‘no IA’ refers to the case where we assume there to be no selection effect by setting $(\eta\chi)_{\text{eff}} = 0$, while in all other cases we do account for the selection effect. The prior on \tilde{C}_1 is based on [Singh et al. \(2015\)](#).

is generally neglected ([Martens et al., 2018](#)). It is then sufficient to use only two observables to constrain b_g and f , which are usually the mono- and quadrupole moments of P_{gg} ([Blake et al., 2018](#)).

The results for this case are summarized in Figure (5), and in the first scenario of Table II. We see that we get very low fractional errors for both free parameters in this case, which confirms that we can constrain both parameters very well using only P_{gg} if we neglect intrinsic alignment effects. However, it is important to emphasize here that this result is obtained using an incorrect model. One cannot simply choose to ‘turn off’ the orientation-dependent selection effect; it is an unavoidable physical phenomenon. By neglecting it we are actually getting a measurement on $f + A$ instead of f , and $b_g - A/3$ instead of b_g . Because of this bias the actual values of b_g and f are shifted with respect to their fiducial values. A simple extension of the Fisher formalism allows one to calculate this shift due to systematic bias, which is described in [Amara and Réfrégier \(2008\)](#). The result of this calculation is shown in the right panel of Figure (5), where the blue ellipse shows how the parameters are shifted with respect to their fiducial values due to intrinsic alignment effects.

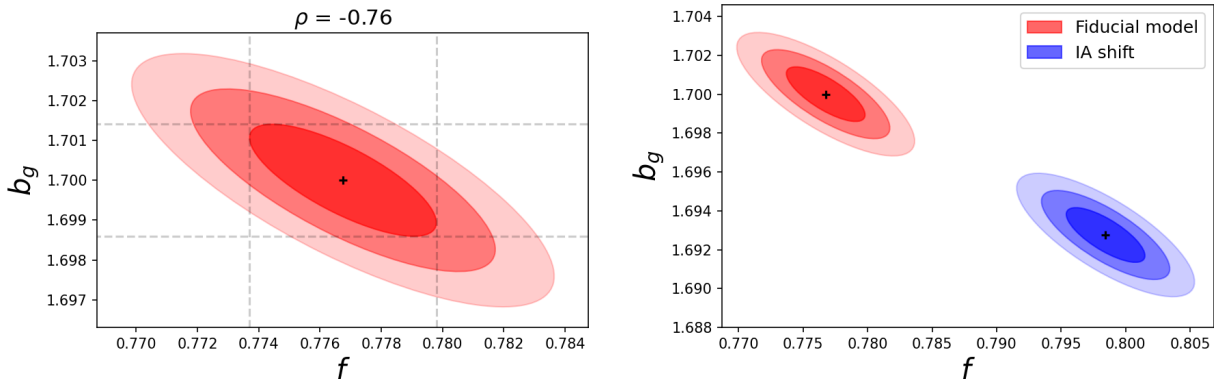


Figure 5: The confidence ellipse (left panel) for b_g and f using $P_{gg}^{(0)}$ and $P_{gg}^{(2)}$ as observables, without including the selection effect. The Pearson correlation coefficient is given by ρ . In the right panel, we show the shift with respect to the fiducial values induced by intrinsic alignment (IA) effects.

4.2 With selection effect

By taking into account the selection effect, P_{gg} gains a dependency on \tilde{C}_1 which is in principle a free parameter. We can then no longer constrain all three free parameters using the same two observables, namely $P_{gg}^{(0)}$ and $P_{gg}^{(2)}$, without additional information. Adding $P_{gg}^{(4)}$ would not resolve this issue because of the degeneracy that arises; the free parameters are fully correlated and can only be disentangled using a different power spectrum. There are several cases which are discussed that allow us to break the degeneracy: adding a prior on \tilde{C}_1 , adding $P_{EE}^{(0)}$, adding $P_{gE}^{(0)}$, or adding both $P_{EE}^{(0)}$ and $P_{gE}^{(0)}$.

4.2.1 Prior on \tilde{C}_1

If we have some prior information on the value and error of \tilde{C}_1 , we can add this to our Fisher matrix and thereby partially constrain this parameter. Doing so allows us to get constraints for all three parameters using only $P_{gg}^{(0)}$ and $P_{gg}^{(2)}$. We use the fractional error found by Singh et al. (2015) as our prior: $\delta\tilde{C}_1/\tilde{C}_1 \approx 0.109$. The confidence ellipses that come out of this scenario are shown in Figure (6), and the fractional errors in the second scenario of Table II.

4.2.2 Adding $P_{EE}^{(0)}$

Instead of using a prior from another study, we can also leave \tilde{C}_1 completely free and get our own constraint on it by adding another observable which depends on this parameter. We can choose $P_{gg}^{(0)}$, $P_{gg}^{(2)}$, and $P_{EE}^{(0)}$ as our observables and let all three parameters vary freely. The confidence ellipses for this scenario are shown in Figure (7), and the fractional errors in the third scenario of Table II.

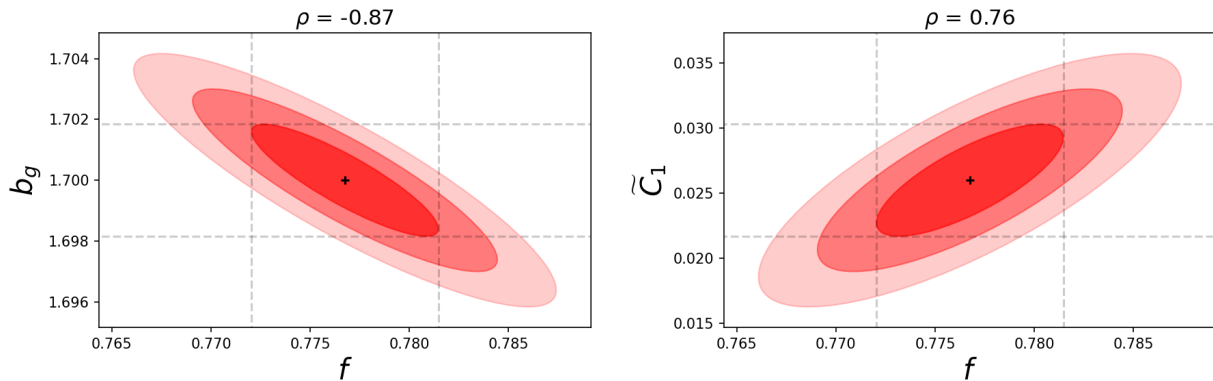


Figure 6: The confidence ellipses for b_g , f , and \tilde{C}_1 using $P_{gg}^{(0)}$, $P_{gg}^{(2)}$ and a prior from Singh et al. (2015).

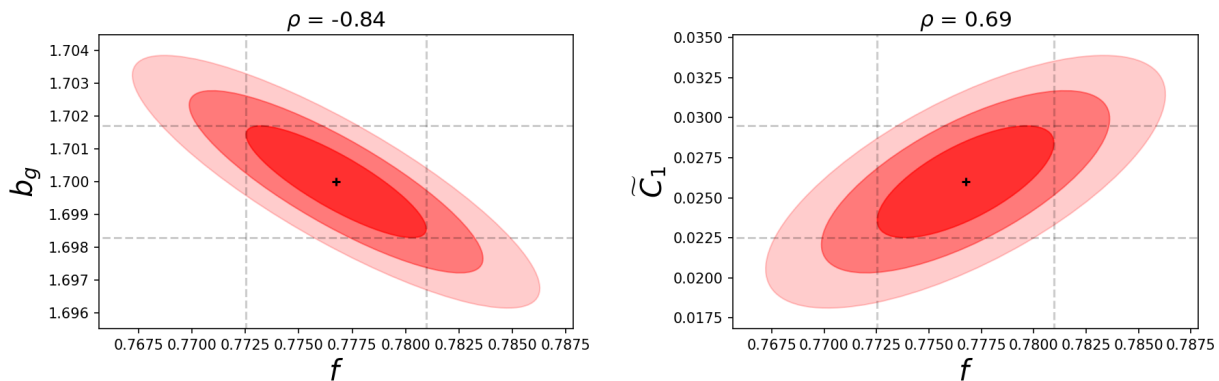


Figure 7: The confidence ellipses for b_g , f , and \tilde{C}_1 using $P_{gg}^{(0)}$, $P_{gg}^{(2)}$ and $P_{EE}^{(0)}$ as observables.

4.2.3 Adding $P_{gE}^{(0)}$

Alternatively, we could use $P_{gE}^{(0)}$ instead of $P_{EE}^{(0)}$ as our additional observable. The results for this scenario are summarized in Figure (8) and the fourth scenario in Table II.

4.2.4 Adding both $P_{EE}^{(0)}$ and $P_{gE}^{(0)}$

Adding both intrinsic alignment power spectra does not significantly improve the constraints with respect to adding only $P_{gE}^{(0)}$. The confidence ellipses are indistinguishable from Figure (8) and are therefore not included. This scenario is also omitted in Table II because the fractional errors are the same as the previous scenario up to at least three significant figures.

5 Discussion

In this section we discuss and interpret the results of the Fisher forecast, as well as explore possible limitations of our analysis.

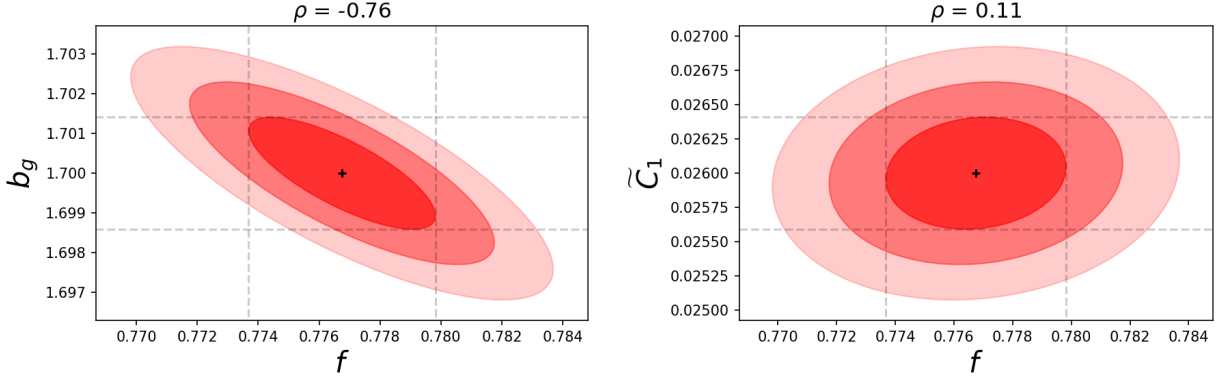


Figure 8: The confidence ellipses for b_g , f , and \tilde{C}_1 using $P_{gg}^{(0)}$, $P_{gg}^{(2)}$ and $P_{gE}^{(0)}$ as observables.

5.1 Interpretation of results

Intrinsic alignment effects on galaxy spectroscopic surveys are typically neglected when constraining the growth rate using RSD measurements. We explored this reference scenario in section 4.1 by setting $(\eta\chi)_{\text{eff}} = 0$, and we indeed find that we get very good constraints on both b_g and f . However, as discussed in section 2.3.3, this model is incorrect because in general there *is* an orientation-dependent selection effect ($(\eta\chi)_{\text{eff}} \neq 0$) that will alter the expression for P_{gg} . In particular, we found that $b_g \rightarrow b_g - R\tilde{C}_1/3$ and $f \rightarrow f + R\tilde{C}_1$. This implies that the constraint we get on f in section 4.1 is actually a constraint on $f + R\tilde{C}_1$, which results in the shift with respect to the fiducial value shown in the right panel of Figure (5). For the fiducial value we are using the contamination of f is about $|R\tilde{C}_1|/f \approx 0.028$, which is small but significant for precision cosmology. Hirata (2009) predicts that this contamination could rise to 10% in certain cases. In order to break this degeneracy, additional information is needed.

In section 4.2 we explore four possible pathways to constrain \tilde{C}_1 and thereby mitigate the impact on our constraints on f . Firstly, we add a prior constraint on \tilde{C}_1 from Singh et al. (2015), which allows us to still only use $P_{gg}^{(0)}$ and $P_{gg}^{(2)}$ as our observables. This gives reasonably good constraints on all three parameters, although they are somewhat larger than in the reference case. From the ellipse plots it can also be seen that the parameters are quite correlated. We get slightly better results if we do not add a prior but instead add $P_{EE}^{(0)}$ as an observable. However, adding $P_{gE}^{(0)}$ instead gives us much better results, which makes sense given that this observable has less noise than $P_{EE}^{(0)}$. The constraints on b_g and f are nearly the same as in the reference case, and we also get a much better constraint on \tilde{C}_1 . Furthermore, in Figure (8) we see that the correlation between f and \tilde{C}_1 is much closer to zero, which clearly indicates that the degeneracy between these two parameters has been broken. Adding both $P_{EE}^{(0)}$ and $P_{gE}^{(0)}$ does not significantly improve the constraints compared to using only $P_{gE}^{(0)}$, which makes this scenario undesirable since adding unnecessary observables will just make the analysis more computationally expensive.

Based on these results we can conclude that although additional observables or priors are needed to account for the selection effect, its impact on the constraints for the growth rate can be mitigated effectively by including galaxy alignment statistics. In particular P_{gE} has

proven to be effective in breaking the degeneracy between f and \tilde{C}_1 . This is advantageous since P_{gE} has less noise and is easier to measure compared to P_{EE} (Taruya and Okumura, 2020). It is also worth mentioning that all constraints improve significantly as the value of k_{\max} increases. This is to be expected since it implies we are adding more k -modes and thus more data to our analysis. This suggests that extending our forecast into the nonlinear regime could be worth the effort. In this case, it would also be interesting to investigate the effect of adding higher order multipole moments of the intrinsic alignment power spectra to the forecast, which was not done in this thesis.

5.2 Further considerations

Although the results of the Fisher forecast are promising, there are a couple of key assumptions that were made that are worth discussing in more detail. Most notable is the fact that we have assumed complete knowledge about $(\eta\chi)_{\text{eff}}$ through η and χ , which allowed us to rewrite A in terms of only one free parameter, \tilde{C}_1 . The values for η and χ were taken from Hirata (2009), but the author emphasized that these were very rough estimates. In general these parameters will depend on the specifics of the survey and will have some uncertainty; establishing these values more accurately and with appropriate uncertainties would require further analysis. In a more realistic scenario one would incorporate the errors on these parameters as priors in the Fisher analysis so that their uncertainty is reflected in the constraints on the other parameters, most importantly the growth rate. The fact that we have not done this means our results are optimistically biased.

Another way to approach this issue would be to not rewrite A at all but to instead leave it as a new free parameter. This would of course mean that we are unable to constrain it through any of the E -mode statistics since the relationship to \tilde{C}_1 would not be established. A potential alternative way of breaking the degeneracy could then be by including additional power spectra from the large-scale velocity field. In van Gemenen and Chisari (2020) they find that the signal in such velocity statistics is significant enough to be detectable in upcoming surveys. These power spectra can be derived using Eq. (14):

$$P_{v_r v_r}(k, \mu) = \left(\frac{\mu b_v f a H}{k} \right)^2 P_{\delta\delta}(k) \quad (52)$$

$$P_{v_r E}(k, \mu) = -\tilde{C}_1 f a H (1 - \mu^2) \mu \frac{1}{k} P_{\delta\delta}(k) \quad (53)$$

where the extra factor of μ comes from the fact that we are considering only the radial component of the velocity field, and b_v is a bias factor that comes from the reconstruction of the velocity field (van Gemenen and Chisari, 2020). The reason that these power spectra could be really useful is the fact that the velocity field also depends on the growth rate f , but not through δ_g . It therefore ‘escapes’ the selection effect and gives us a way of constraining f that is independent of A . This property could be used to break the degeneracy between f and A and provide a way to constrain A independent of \tilde{C}_1 . This approach was also attempted in this thesis but did not succeed due to numerical instabilities that would require further research.

Another important consideration that has not yet been discussed is the assumption that galaxy shape statistics are not affected by the orientation-dependent selection effect. Intuitively, one might expect that E -mode statistics are similarly biased towards galaxies which are aligned along the line of sight, for the simple reason that they are observed more easily than perpendicularly aligned galaxies. This is in fact true, but at large (linear) scales this effect may be neglected (Hirata and Seljak, 2004). We can only observe galaxy shapes where there are galaxies, so the intrinsic shape field that we observe is inherently biased by the galaxy density field. What is actually observed is then a density-weighted intrinsic shape, given by $\tilde{\gamma} = (1 + \delta_g)\gamma$ Kurita et al. (2020). However, because γ is proportional to the matter density field δ (see Eq. (21)), at linear scales we may write $\tilde{\gamma} \approx \gamma$ (Blazek et al., 2011). In case one would want to extend this analysis to nonlinear scales the δ_g -dependency could no longer be neglected, and through δ_g the selection effect and thus A would also appear in the intrinsic alignment statistics.

6 Conclusion

In this thesis the effect of galaxy intrinsic alignments on RSD measurements is investigated. Through RSD effects, galaxy clustering statistics act as a powerful observational probe of cosmological parameters, most notably the growth rate. Galaxy orientations and their alignments are typically not taken into account in these measurements, which turns out to be problematic because of two reasons: galaxy orientations are not random but are correlated with one another, *and* there is an orientation-dependent selection effect which biases our data in favor of galaxies aligned along the line of sight. This selection effect anisotropically distorts the galaxy clustering power spectrum and thereby mimics RSD effects, making their contributions difficult to disentangle. By assuming a linear alignment model we have shown that this results in $b_g \rightarrow b_g - A/3$ and $f \rightarrow f + A$, and that we can rewrite A as $A = -3.48(\eta\chi)_{\text{eff}} \tilde{C}_1$.

There is a degeneracy between the parameters that cannot be broken using P_{gg} alone. We use a Fisher forecast to predict how well future surveys could mitigate this selection effect using additional observables which involve intrinsic alignment statistics. We conclude that using P_{gE} , specifically its monopole moment, in addition to the usual galaxy clustering statistics is most effective in constraining the free parameters b_g , f , and \tilde{C}_1 , and the correlations between them. In this scenario we find that the constraints on b_g and f are almost the same as in the usual case where the selection effect is neglected. In other words, although intrinsic alignments do distort our measurements of the growth rate through RSD effects, we can recover good constraints on f by including additional intrinsic alignment observables.

The most notable assumption that we have made in our analysis comes in through the relation between A and \tilde{C}_1 , where we assumed complete knowledge on $(\eta\chi)_{\text{eff}}$, which represent the selection effect contribution to A . This effectively describes how the number of observed galaxies changes as a function of their alignment with respect to the line of sight. We have assumed some rough estimate for these parameters based on Hirata (2009), but for a more realistic assessment further research into these parameters and their uncertainties would be required. Alternatively, it could be worthwhile to bring in large-scale velocity statistics in order to constrain f independently of the galaxy density field, as suggested by van Gemenen

and Chisari (2020). This would allow for a measure of f that circumvents the selection effect.

In general, it is important to keep in mind that throughout this thesis we have made approximations that are only valid up to linear order, thus at large scales. As new surveys venture into the nonlinear regime it will become more important to investigate how we could extend our models beyond linear theory. This is especially significant given that all constraints seem to decrease as a function of k_{max} . Regardless of these assumptions, it is clear that galaxy intrinsic alignments do impact galaxy clustering statistics and therefore also our measurements on key cosmological parameters such as the growth rate. For that reason it is important to start integrating intrinsic alignment statistics into our toolbox for studying the large-scale structure of the Universe.

References

- B. Ryden, *Introduction to Cosmology* (Cambridge University Press, 2017), 2nd ed.
- LSST DESC, R. Mandelbaum, T. Eifler, R. Hložek, T. Collett, E. Gawiser, D. Scolnic, D. Alonso, H. Awan, R. Biswas, et al., *The lsst dark energy science collaboration (desc) science requirements document* (2018), [1809.01669](https://doi.org/10.1186/1525.01669).
- S. Dodelson and F. Schmidt, *Modern Cosmology* (Academic Press, 2020), 2nd ed.
- H. Gil-Marín, W. J. Percival, L. Verde, J. R. Brownstein, C.-H. Chuang, F.-S. Kitaura, S. A. Rodríguez-Torres, and M. D. Olmstead, *Monthly Notices of the Royal Astronomical Society* **465**, 1757–1788 (2016), ISSN 1365-2966, URL <http://dx.doi.org/10.1093/mnras/stw2679>.
- P. Catelan, M. Kamionkowski, and R. D. Blandford, *Monthly Notices of the Royal Astronomical Society* **320**, L7–L13 (2001), ISSN 1365-2966, URL <http://dx.doi.org/10.1046/j.1365-8711.2001.04105.x>.
- C. M. Hirata, *Monthly Notices of the Royal Astronomical Society* **399**, 1074 (2009), ISSN 0035-8711, <https://academic.oup.com/mnras/article-pdf/399/2/1074/3662737/mnras0399-1074.pdf>, URL <https://doi.org/10.1111/j.1365-2966.2009.15353.x>.
- D. Martens, C. M. Hirata, A. J. Ross, and X. Fang, *Monthly Notices of the Royal Astronomical Society* **478**, 711–732 (2018), ISSN 1365-2966, URL <http://dx.doi.org/10.1093/mnras/sty1100>.
- S. Singh, B. Yu, and U. Seljak, *Monthly Notices of the Royal Astronomical Society* **501**, 4167–4183 (2020), ISSN 1365-2966, URL <http://dx.doi.org/10.1093/mnras/staa3263>.
- E. Hubble, *Proceedings of the National Academy of Sciences* **15**, 168 (1929), ISSN 0027-8424, <https://www.pnas.org/content/15/3/168.full.pdf>, URL <https://www.pnas.org/content/15/3/168>.
- A. A. Penzias and R. W. Wilson, **142**, 419 (1965).

- R. H. Dicke, P. J. E. Peebles, P. G. Roll, and D. T. Wilkinson, **142**, 414 (1965).
- G. F. Smoot, C. L. Bennett, A. Kogut, E. Wright, J. Aymon, N. Boggess, E. Cheng, G. De Amici, S. Gulkis, M. Hauser, et al., *The Astrophysical Journal* **396**, L1 (1992).
- V. C. Rubin and W. K. Ford Jr, *The Astrophysical Journal* **159**, 379 (1970).
- D. Clowe, M. Bradač, A. H. Gonzalez, M. Markevitch, S. W. Randall, C. Jones, and D. Zaritsky, *The Astrophysical Journal* **648**, L109–L113 (2006), ISSN 1538-4357, URL <http://dx.doi.org/10.1086/508162>.
- A. G. Riess, A. V. Filippenko, P. Challis, A. Clocchiatti, A. Diercks, P. M. Garnavich, R. L. Gilliland, C. J. Hogan, S. Jha, R. P. Kirshner, et al., *The Astronomical Journal* **116**, 1009–1038 (1998), ISSN 0004-6256, URL <http://dx.doi.org/10.1086/300499>.
- Planck Collaboration, N. Aghanim, Y. Akrami, M. Ashdown, J. Aumont, C. Baccigalupi, M. Ballardini, A. J. Banday, R. B. Barreiro, N. Bartolo, et al., *Planck 2018 results. vi. cosmological parameters* (2020), **1807.06209**.
- M. J. Mortonson, D. H. Weinberg, and M. White, arXiv e-prints arXiv:1401.0046 (2013), **1401.0046**.
- D. J. Eisenstein, I. Zehavi, D. W. Hogg, R. Scoccimarro, M. R. Blanton, R. C. Nichol, R. Scranton, H. Seo, M. Tegmark, Z. Zheng, et al., *The Astrophysical Journal* **633**, 560–574 (2005), ISSN 1538-4357, URL <http://dx.doi.org/10.1086/466512>.
- N. Kaiser, *Monthly Notices of the Royal Astronomical Society* **227**, 1 (1987), ISSN 0035-8711, <https://academic.oup.com/mnras/article-pdf/227/1/1/18522208/mnras227-0001.pdf>, URL <https://doi.org/10.1093/mnras/227.1.1>.
- A. J. S. Hamilton, **385**, L5 (1992).
- J. Richard, J.-P. Kneib, C. Blake, A. Raichoor, J. Comparat, T. Shanks, J. Sorce, M. Sahlén, C. Howlett, E. Tempel, et al., arXiv preprint arXiv:1903.02474 (2019).
- S. Singh, R. Mandelbaum, and S. More, *Monthly Notices of the Royal Astronomical Society* **450**, 2195–2216 (2015), ISSN 0035-8711, URL <http://dx.doi.org/10.1093/mnras/stv778>.
- T. Okumura, A. Taruya, and T. Nishimichi, *Physical Review D* **100** (2019), ISSN 2470-0029, URL <http://dx.doi.org/10.1103/PhysRevD.100.103507>.
- T. Kurita, M. Takada, T. Nishimichi, R. Takahashi, K. Osato, and Y. Kobayashi, *Power spectrum of halo intrinsic alignments in simulations* (2020), **2004.12579**.
- I. van Gemeren and N. Chisari, *Physical Review D* **102** (2020), ISSN 2470-0029, URL <http://dx.doi.org/10.1103/PhysRevD.102.123507>.

- J. Blazek, M. McQuinn, and U. Seljak, *Journal of Cosmology and Astroparticle Physics* **2011**, 010–010 (2011), ISSN 1475-7516, URL <http://dx.doi.org/10.1088/1475-7516/2011/05/010>.
- A. Taruya and T. Okumura, *The Astrophysical Journal* **891**, L42 (2020), ISSN 2041-8213, URL <http://dx.doi.org/10.3847/2041-8213/ab7934>.
- B. Joachimi, R. Mandelbaum, F. B. Abdalla, and S. L. Bridle, *Astronomy Astrophysics* **527**, A26 (2011), ISSN 1432-0746, URL <http://dx.doi.org/10.1051/0004-6361/201015621>.
- T. Okumura, A. Taruya, and T. Nishimichi, *Monthly Notices of the Royal Astronomical Society* **494**, 694–702 (2020), ISSN 1365-2966, URL <http://dx.doi.org/10.1093/mnras/staa718>.
- Y. Kobayashi, T. Nishimichi, M. Takada, and R. Takahashi, *Cosmological information content in redshift-space power spectrum of sdss-like galaxies in the quasi-nonlinear regime up to $k = 0.3 h \text{ mpc}^{-1}$* (2020), [1907.08515](https://arxiv.org/abs/1907.08515).
- C. Blake, P. Carter, and J. Koda, *Monthly Notices of the Royal Astronomical Society* **479**, 5168–5183 (2018), ISSN 1365-2966, URL <http://dx.doi.org/10.1093/mnras/sty1814>.
- D. Coe, *Fisher matrices and confidence ellipses: A quick-start guide and software* (2009), [0906.4123](https://arxiv.org/abs/0906.4123).
- F. Schmidt, N. E. Chisari, and C. Dvorkin, *Journal of Cosmology and Astroparticle Physics* **2015**, 032–032 (2015), ISSN 1475-7516, URL <http://dx.doi.org/10.1088/1475-7516/2015/10/032>.
- C. A. J. Duncan, B. Joachimi, A. F. Heavens, C. Heymans, and H. Hildebrandt, *Monthly Notices of the Royal Astronomical Society* **437**, 2471–2487 (2013), ISSN 1365-2966, URL <http://dx.doi.org/10.1093/mnras/stt2060>.
- Ž. Ivezić, S. M. Kahn, J. A. Tyson, B. Abel, E. Acosta, R. Allsman, D. Alonso, Y. AlSayyad, S. F. Anderson, J. Andrew, et al., *The Astrophysical Journal* **873**, 111 (2019).
- N. E. Chisari, D. Alonso, E. Krause, C. D. Leonard, P. Bull, J. Neveu, A. Villarreal, S. Singh, T. McClintock, J. Ellison, et al., **242**, 2 (2019), [1812.05995](https://arxiv.org/abs/1812.05995).
- A. Amara and A. Réfrégier, *Monthly Notices of the Royal Astronomical Society* **391**, 228–236 (2008), ISSN 1365-2966, URL <http://dx.doi.org/10.1111/j.1365-2966.2008.13880.x>.
- C. M. Hirata and U. Seljak, **70**, 063526 (2004), [astro-ph/0406275](https://arxiv.org/abs/astro-ph/0406275).